Secondary Organic Aerosols Derived from Intermediate Volatility n-Alkanes Adopt Low Viscous Phase State

Tommaso Galeazzo[1], Bernard Aumont[2], Marie Camredon[2], Richard Valorso[2], Yong B. Lim[3], Paul J. Ziemann[4,5], and Manabu Shiraiwa[1,*]

1. Department of Chemistry, University of California, Irvine, CA92625, USA

2. Univ Paris Est Creteil and Université Paris Cité, CNRS, LISA, F-94010 Créteil, France

3. California Air Resources Board, Riverside, CA92507, USA

4. Department of Chemistry, University of Colorado, Boulder, Colorado, USA

5. Cooperative Institute for Research in Environmental Sciences (CIRES), University of Colorado, Boulder, Colorado, USA

* Correspondence to: m.shiraiwa@uci.edu

Abstract.

Secondary organic aerosol (SOA) derived from n-alkanes, as emitted from vehicles and volatile chemical products, is a major component of anthropogenic particulate matter, yet the chemical composition and phase state are poorly understood and thus poorly constrained in aerosol models. Here we provide a comprehensive analysis of n-alkane SOA by explicit gas-phase chemistry modeling, machine learning, and laboratory experiments to show that n-alkane SOA adopt low viscous semisolid or liquid states. Our study underlines the complex interplay of molecular composition and SOA viscosity: n-alkane SOA with higher carbon number mostly consists of less functionalized first-generation products with lower viscosity, while the lower carbon number SOA contains more functionalized multigeneration products with higher viscosity. This study opens up a new avenue for analysis of SOA processes and the results indicate little kinetic limitations of mass accommodation in SOA formation, supporting the application of equilibrium partitioning for simulating n-alkane SOA formation in large-scale atmospheric models.

Introduction

Secondary organic aerosol (SOA) is ubiquitous in the atmosphere, affecting climate, air quality and public health (Pöschl and Shiraiwa, 2015; Jimenez et al., 2009). They are generally formed by multigenerational oxidation of volatile organic compounds (VOCs) emitted by both anthropogenic and biogenic sources followed by condensation of semi-volatile oxidation products into the particle phase (Ziemann and Atkinson, 2012; Kroll and Seinfeld, 2008). As an important class of SOA precursors, there is a growing attention to intermediate volatile organic compounds (IVOCs), which can partition to the gas phase upon dilution of primary organic aerosols after fresh emission sources such as vehicle tailpipes, combustion of fossil and fuel oils, and volatile chemical products (Robinson et al., 2007; McDonald et al., 2018). The inclusion of IVOCs in the model simulations helps to reduce the gap between model simulation and field observation of SOA (de Gouw et al., 2011; Li et al., 2022; Zhao et al., 2016).

SOA can adopt different particle phase states (liquid, amorphous semisolid, and glassy solid), depending on their chemical composition, relative humidity and temperature (Virtanen et al., 2010; Petters et al., 2019; Reid et al., 2018; Renbaum-Wolff et al., 2013) and also evolving upon chemical aging and photochemistry (Baboomian et al., 2022). SOA phase state plays an important role in a number of atmospheric multiphase processes (Shiraiwa et al., 2017). The occurrence of glassy SOA in the free troposphere can impact activation pathways of ice crystals and cloud droplets (Knopf and Alpert, 2023). Slow diffusion in viscous particles

induces kinetic limitations in heterogeneous and multiphase reactions (Zhang et al., 2018; Zhou et al., 2019; Shiraiwa et al., 2011), affecting long-range transport (Shrivastava et al., 2017; Mu et al., 2018). The timescale of SOA partitioning can be prolonged in viscous particles (Schervish and Shiraiwa, 2023), retarding uptake of semi-volatile compounds and mixing of different particle populations (Ye et al., 2016). Particle phase state also modulates SOA growth to cloud condensation nuclei sizes, affecting cloud life cycle (Zaveri et al., 2022). While the phase states of SOA generated by biogenic VOCs such as terpenes and isoprene have been extensively studied (Virtanen et al., 2010; Petters et al., 2019; Renbaum-Wolff et al., 2013; Baboomian et al., 2022; Zhang et al., 2018), those derived from IVOCs are hardly investigated and remain poorly constrained.

Viscosity (η) is a dynamic property that characterizes the particle phase state, which can be derived from the glass transition temperature (T_g) of the constituting species (Koop et al., 2011). Several structure-activity relationships models have been developed to predict the T_g of an organic compound using various molecular properties including molar mass, atomic O:C ratio (Shiraiwa et al., 2017), elemental composition (DeRieux et al., 2018), and volatility (Li et al., 2020; Zhang et al., 2019). A method was developed to predict SOA viscosity from the T_g-scaled Arrhenius plot of fragility by considering Gordon-Taylor mixing rule and hygroscopic growth of SOA particles (DeRieux et al., 2018; Shiraiwa et al., 2017). The T_g compositional parameterizations (CP) and the viscosity prediction method have been applied to high resolution mass spectrometry data of various types of SOA including toluene SOA (DeRieux et al., 2018), SOA generated by diesel fuels (Song et al., 2019), β-caryophyllene SOA (Maclean et al., 2021), and SOA generated by surrogate VOC mixtures by healthy and stressed plants (Smith et al., 2021), agreeing well with viscosity measurements. However, CP substantially overestimated viscosity measurements of indoor surface films which are mostly composed of unsaturated high molar mass compounds such as triglycerides (O'Brien et al., 2021). CP does not consider molecular structure nor functionality explicitly, representing a limitation of this method. Galeazzo and Shiraiwa (2022) overcame this limitation by developing a machine learning-based model, tgBoost, with an application of cheminformatics "molecular embeddings" that retains detailed information on atomic composition, molecular structure and connectivity. The main novel feature introduced by tgBoost is model capability to predict different T_g for structural isomers and high sensitivity of T_g to various functional groups, consistent with viscosity measurements for functionalized compounds (Rothfuss and Petters, 2017; Grayson et al., 2017).

84   Long-chain linear alkanes (n-alkanes) are representative IVOCs and account for a

85   substantial fraction of non-methane hydrocarbons in urban air as mainly emitted from

86   anthropogenic activities such as vehicle exhausts and incomplete fuel combustion (Li et al.,

87   2022). Gas-phase oxidation of n-alkanes by OH radicals can trigger the formation of SOA with

88   high yields, as observed in laboratory experiments (Aimanant and Ziemann, 2013a; Lim and

89   Ziemann, 2009b; Srivastava et al., 2022) and field observations (Gentner et al., 2012; Li et al.,

90   2022). Gas-phase oxidation pathways of n-alkanes are relatively well understood and

91   successfully simulated by detailed gas-phase chemistry modeling (Aumont et al., 2012; La et

92   al., 2016), but the chemical composition of n-alkane SOA has only been characterized well for

93   the C_{16} n-alkane (Ranney et al., 2023) and the phase state and viscosity of alkane SOA are

94   unknown. Therefore, the n-alkane SOA system provides an ideal benchmark for the

95   investigation of the interplay of chemical composition, particle phase state and kinetic

96   limitations influencing SOA growth and evolution.

97   In this study, we implemented tgBoost in an explicit gas-phase chemistry model

98   GECKO-A to investigate the complex interplay of chemical composition, kinetic partitioning,

99   and phase state of n-alkane SOA generated under dry and high NOx conditions. The GECKO-

100   A model is one of the most comprehensive generators of gas-phase chemical schemes to date,

101   as it automatically generates detailed gas-phase chemical mechanisms involving thousands to

102   millions of oxidation products from a given VOC precursor based on established reaction

103   pathways and structure–activity relationships (Aumont et al., 2012; La et al., 2016). The

104   simulations were conducted with variable effective mass accommodation coefficient to

105   consider potential kinetic limitations in amorphous semisolid particles (Shiraiwa and Pöschl,

106   2021). The simulated results were compared with chamber experimental data on SOA yields

107   (Lim and Ziemann, 2009b) as well as new measurements on thermal desorption temperatures

108   and functional group distributions.

109

110   **Methods:**

111   **Model simulations.**

112   We applied the Generator for Explicit Chemistry and Kinetics of the Organics in the

113   Atmosphere (GECKO-A) (Aumont et al., 2012; La et al., 2016) to obtain detailed reaction

114   schemes of gas-phase OH oxidation of n-alkanes along with rate constants. The GECKO-A

115   generator used for the oxidation of linear n-alkanes treats chemistry of peroxy (RO_2) and alkoxy

116   (RO) radicals. Under high NOx conditions, RO_2 radicals mainly react with NO and NO_2, to

117   form closed-shell compounds or RO radicals, which undergo reaction with O_2, unimolecular

118 decomposition (i.e. C-C bond breaking) or isomerization, generating stable compounds and/or

119 to new RO_2 radicals. The detailed protocol for such mechanism generation is available in

120 previous studies (Aumont et al., 2013; Aumont et al., 2005; Aumont et al., 2012; La et al.,

121 2016). In this study, the generated chemical schemes include the description of the formation

122 of organic species up to four generations. Species with vapor pressure below 10^{-13} atm are

123 assumed to be of low enough volatility to completely partition to the condensed phase and their

124 gas phase chemistry is then not generated in the mechanism to reduce the mechanism (La et al.,

125 2016). The number of species treated in the model was $\sim 10^4$ species for dodecane (C_8H_{18}) that

126 increases to $\sim 10^5$ species for heptadecane ($C_{17}H_{36}$).

127   The latest structure-activity relationships are treated for the chemistry of organic

128 compounds with OH radical (Jenkin et al., 2018b, a; Jenkin et al., 2019), the bimolecular

129 reactions of peroxy radicals (Jenkin et al., 2019), as well as alkoxy radical decomposition and

130 H migration reaction rates (Vereecken and Peeters, 2009; La et al., 2016). The vapor pressures

131 of semi-volatile species were estimated by using Nannoolal's group contribution method

132 (Nannoolal et al., 2008) implemented in GECKO-A, as described in detail in Valorso et al.

133 (2011). The model treats unimolecular particle-phase reactions including cyclization of

134 hydroxyketones and dehydration of cyclic hemiacetals to form dihydrofurans (La et al., 2016).

135 The model does not treat autoxidation and dimerization in the gas phase, but these processes

136 should be minor pathways during n-alkane oxidation in the presence of high NOx as the reaction

137 of peroxy radicals with NOx should be dominant (Praske et al., 2018; Pye et al., 2019); thus,

138 their absence from GECKO-A chemical schemes should not have major impacts on the

139 simulated results.

140   These explicit chemical mechanisms were implemented into a box model to simulate

141 the multigenerational oxidation of n-alkanes, partitioning of oxidation products into the particle

142 phase based on their vapor pressures, and vapor wall loss to mimic chamber experiments (La

143 et al., 2016). We replicated the experimental conditions used in Lim and Ziemann (2009b) to

144 generate SOA from OH oxidation of C_8-C_{17} n-alkanes at high NO_x conditions in the presence

145 of non-volatile dioctyl sebacate (DOS) seed particles with particle radius of 150 nm and mass

146 loading of 200 $\mu g\ m^{-3}$. Temperature was held constant at 295.15 K, pressure was set at 1 atm

147 and RH was fixed at 0.5%. Photolysis frequencies were calculated based on the cross sections,

148 quantum yields as described in Aumont et al. (2005) and the photonic flux of blacklight lamps.

149 Each simulation ran for 1 hour and the time evolution of species concentration were computed

150 through a two-step method that solves stiff ordinary differential equations (Verwer, 1994;

151 Verwer et al., 1996). To investigate effects of mass concentrations, we also simulated

152 experiments of n-alkane photooxidation under high NO_x conditions with low mass loadings by

153 Presto et al. (2010). The number concentration of seed particles with particle diameter of 200

154 nm was ~5000 cm^{-3}, corresponding to the mass concentration of ~20 μg m^{-3}. Initial mixing

155 ratios of n-alkane and NO_x were in the range of 3 – 99 ppb and 1 – 5 ppm, respectively, as

156 reported in Presto et al. (2010) and these conditions were applied in the model.

157   The box model accounts for mass transfer kinetics of organic species between gas and

158 particle phases. Partitioning follows Raoult's law at equilibrium and partitioning kinetics are

159 described by the gas-particle mass transfer coefficient with the Fuchs-Sutugin approach

160 (Seinfeld and Pandis, 2016). For the base case scenario, we fixed the mass accommodation

161 coefficient (α) to be 1 based on molecular dynamics simulations (Julin et al., 2014), assuming

162 particles being low viscous liquids without kinetic limitations of bulk diffusion. To account for

163 potential kinetic limitations in viscous particles, we applied an effective mass accommodation

164 coefficient (α_{eff}) that is a function of volatility and bulk diffusivity (Shiraiwa and Pöschl, 2021):

$$\alpha_{eff} = \alpha_s \frac{1}{1 + \frac{\alpha_s\,\omega\,C^0}{4\,D_b\,\rho_p}\frac{r_p}{5}\cdot 10^{-12}\frac{g\ cm^{-3}}{\mu g\ m^{-3}}} \qquad (1)$$

166 where α_s is the surface accommodation coefficient assumed to be 1, ω (cm s^{-1}) is the mean

167 thermal velocity of the organic compound in the gas phase, r_P (cm) is the particle radius, ρ_p (g

168 cm^{-3}) is the particle density, and C^0 (μg m^{-3}) is the pure compound saturation mass

169 concentration. D_b ($cm^2\ s^{-1}$) is bulk diffusivity as simulated by conversion of viscosity as detailed

170 below. α_{eff} values are shown as a function of D_b and vapor pressure p^o in Fig A3a. We

171 accounted for a reversible gas-to-chamber wall partitioning of gases and assumed a fixed first-

172 order deposition rate constant of 5×10^{-4} s^{-1} based on experimental observations and previous

173 modeling studies (Krechmer et al., 2016; La et al., 2016; Lim and Ziemann, 2009b). A

174 desorption rate constant from wall to the gas phase was derived by using a parameter of

175 $C_w/M_w\gamma_w$ of 9 μmole m^{-3} for n-alkanes and 120 μmole m^{-3} for oxidation products based on

176 chamber observations (Matsunaga and Ziemann, 2010), as discussed in La et al. (2016).

177 Potential concentration gradients in the particle phase are not resolved explicitly and SOA

178 particles are assumed to be homogeneously well-mixed.

179   The glass transition temperatures (T_g) of organic compounds were predicted by the

180 machine learning-based model tgBoost (Galeazzo and Shiraiwa, 2022) and the

181 parameterization based on elemental composition (DeRieux et al., 2018; Li et al., 2020). The

182 implementation of the compositional parametrization into the GECKO-A box model was done

183 in Galeazzo et al. (2021) with a thorough description of all the equations, assumptions and steps

184   adopted for the implementation of this viscosity estimation method. In this study, we

185   implemented tgBoost, a newly developed machine learning model for better predictions of T_g.

186   tgBoost is a powerful model that can discern compositional isomers by functionality and predict

187   the glass transition temperature of an organic compound i ($T_{g,i}$) with an uncertainty of $\pm$ 18.3 K

188   using the canonical SMILES notation of a molecule (Galeazzo and Shiraiwa, 2022). We have

189   implemented a pipeline (i.e., gecko2vec) into GECKO-A to predict T_g of compounds from the

190   chemical mechanism in a fast and computationally efficient manner. Gecko2vec executes three

191   main steps: first, it translates the IDs of the compounds of interest of the GECKO-A mechanism

192   into the respective canonical SMILES notations (translation step); second, it transforms the

193   canonical SMILES notations into the respective molecular embeddings (i.e., unique 300-

194   dimensional numerical representations of molecules; embedding step); and finally, the

195   pretrained tgBoost model and its weights are loaded and used to predict T_g of each species

196   (prediction step). Within the box model, the T_g of total SOA particles ($T_{g,org}$) resulting from the

197   combination of its organic component and water mixture is computed using the Gordon–Taylor

198   equation (Dette et al., 2014; Koop et al., 2011; Zobrist et al., 2008). $T_{g,org}$ can be converted to

199   viscosity based on the Vogel-Tammann-Fulcher approach assuming the fragility parameter of

200   10 (DeRieux et al., 2018). Viscosity is further converted into bulk diffusivity using the

201   fractional Stokes-Einstein equation with a fractional parameter of 0.93 and an effective

202   molecular radius of 0.5 nm (Evoy et al., 2019). For both model simulations with CP and

203   tgBoost, the particle number concentration is assumed to remain constant (coagulation is not

204   treated), while the particle radius evolves following the partitioning of organic compounds.

205

206   **Laboratory experiments.**

207   SOA particles were generated from OH oxidation of C_8-C_{17} n-alkanes in a 5.9 m^3 Teflon

208   environmental chamber filled with clean air under high NO_x conditions in the presence of non-

209   volatile dioctyl sebacate (DOS) seed particles, as described in detail elsewhere (Lim and

210   Ziemann, 2009b). Briefly, 1 ppm of n-alkane, 10 ppm of methyl nitrite, and 10 ppm of NO were

211   added to the chamber from a glass bulb, and ~200–400 μg m^{-3} of seed particles were added

212   from an evaporation-condensation apparatus. Relatively high mass concentrations of seed

213   particles were used so that semi-volatile compounds would condense to particles, minimizing

214   vapor deposition to chamber walls (Zhang et al., 2014; Matsunaga and Ziemann, 2010).

215   Blacklights covering two of the chamber walls were then turned on for 60 min to form OH

216   radicals by methyl nitrite photolysis (Atkinson et al., 1981). The amount of n-alkane reacted

217   was measured by collecting Tenax$^®$ samples before and after the experiment and analyzing by

gas chromatography with flame ionization detection (GC-FID). Aerosol volume concentrations were measured using a scanning mobility particle sizer (Docherty et al., 2005) and converted to an SOA mass formed using a density of 1.06 g cm^{-3}. SOA mass yields (mass of SOA formed/mass of n-alkane reacted) were calculated from the measured SMPS mass (corrected for particle wall loss using the ~20% h^{-1} decay in mass after the lights were turned off) and the GC-FID analyses. The final SOA mass concentrations were in the range of ~300 – 6000 μg m^{-3} depending on precursors (Lim and Ziemann, 2009b). The SOA yields measured in these experiments were reported previously (Lim and Ziemann, 2009b), but in light of a recent comparison of the accuracy of our SMPS measurements with filter sampling the values reported here are higher by a factor of 1.24 (Bakker-Arkema and Ziemann, 2021).

A temperature-programmed thermal desorption (TPTD) method was also used to measure thermal desorption temperatures of DOS that was present as seed particles in n-alkane SOA. Particles were sampled directly from the chamber into a thermal desorption particle beam mass spectrometer (Tobias et al., 2000), where they were formed into a beam inside an aerodynamic lens, transported into a high vacuum chamber, and impacted on a copper rod vaporizer that was coated with a non-stick polymer and cooled to –40°C. Note that compounds with vapor pressure <10^{-5} Torr are estimated to undergo negligible evaporation with the residence time of ~0.2 s in the aerodynamic lens (Tobias et al., 2000). After sampling for 30 min, the vaporizer was warmed by room air to –5°C and then heated at 2°C min^{-1} to 200°C. Compounds desorbed according to volatility and entered a quadrupole mass spectrometer, where they were ionized by 70 eV electrons prior to mass analysis. In one recent n-hexadecane experiment, the composition of nitrate, hydroxyl, carbonyl (ketone + aldehyde), carboxylic acid, ester, and peroxide functional groups in SOA was measured using derivatization-spectrophotometric methods, with the amount of -CH$_2$- groups calculated by difference (Ranney et al., 2023). We note that in that experiment the SOA yield measured by filter sampling was nearly identical to the one we measured previously after applying the above correction.

Results and discussion

SOA yields and viscosity.

Figure 1 shows comparisons of measurements and modeling for (a) SOA yields, (b) functional group distributions, (c) N:C ratios, and (d) O:C ratios. Figure 1(a) shows the measured yields of SOA generated from the oxidation of n-alkanes (C_nH_{2n+2}; n = 8 - 17) (Lim and Ziemann, 2009b). The model base case (black line) with mass accommodation coefficient

252   of 1 for all species represents no kinetic limitations in the particle phase and the results are

253   similar to previous simulations performed by La et al. (2016). Vapor wall loss was considered

254   based on experimental observations and previous modeling studies (Krechmer et al., 2016; La

255   et al., 2016; Lim and Ziemann, 2009b), which is important to account for as no wall loss would

256   lead to a significant overestimation of SOA yields, as shown in the black dotted line and was

257   discussed in detail in La et al. (2016). Both experimental and simulated SOA yields increase

258   with an increase of n, reflecting the decrease in volatility of the precursor and its oxidation

259   products (Shiraiwa et al., 2014). The observed SOA yield trend is consistent with measurements

260   by a thermal desorption particle beam mass spectrometer, showing that n-alkane SOA are

261   composed of less oxidized products with lower volatility for precursors with higher n (Lim and

262   Ziemann, 2009b, a).

263   The overall good agreement suggests that multigenerational chemistry in the gas phase

264   and partitioning of semi- and low-volatile products, as explicitly treated by GECKO-A box

265   modeling, are the dominant pathway of n-alkane SOA formation under these conditions. It also

266   suggests that peroxy radicals ($RO_2\cdot$) mainly react with NOx, minimizing autoxidation and gas-

267   phase dimerization by $RO_2\cdot + RO_2\cdot$ reactions. Good model agreement also suggests that particle-

268   phase oligomerization chemistry is not a dominant process, while particle-phase unimolecular

269   reactions including cyclization of hydroxyketones and dehydration of cyclic hemiacetals

270   forming dihydrofurans are treated in the model as they are important for the further oxidation

271   due to the presence of a double bound in the dihydrofurans (Lim and Ziemann, 2009a; La et al.,

272   2016). Thus, the GECKO-A model seemingly treats all essential processes for simulations of

273   n-alkane SOA formation under high NOx conditions. Note that a very recent study suggested

274   that cyclic hemiacetals form acetal dimers in the particle phase for SOA formed from the

275   reaction of n-hexadecane SOA and OH/NOx (Ranney et al., 2023). In addition, particle-phase

276   chemistry was shown to be substantial in n-alkane SOA formation under low NOx conditions

277   through peroxyhemiacetal and oligomer formation (Shiraiwa et al., 2013; Ziemann and

278   Atkinson, 2012). The impact of such particle-phase chemistry may warrant further

279   investigations including model development and experimental studies.

280   To explore the potential impacts of particle phase state on SOA formation and

281   partitioning, we implemented an effective mass accommodation coefficient (α_{eff}) which can

282   effectively consider kinetic limitations of bulk diffusion and also account for the effect of vapor

283   pressure on partitioning kinetics for species with various volatilities (Shiraiwa and Pöschl,

284   2021). Bulk diffusivity evolves upon SOA formation, which can be derived by viscosity and T_g

285   as predicted from the machine learning-based tgBoost model (dashed green line in Fig. 1a) and

the compositional parametrization (CP, dashed orange line in Fig. 1a). The simulated SOA yields with tgBoost are very similar to the base case scenario with $\alpha = 1$, while the application of the CP leads to smaller SOA yields for $n = 15$-17. These results indicate that α_{eff} is close to 1 with little kinetic limitations of bulk diffusion for most cases, except some limitations are predicted by CP for large precursors. Deviations of tgBoost and CP stem from the difference in phase state and viscosity predicted by the two methods.

Figure 2(a) shows the simulated viscosity and corresponding bulk diffusivity of n-alkane SOA. Notably, the two models predict contrasting trends. The simulated glass transition temperature ($T_{g,org}$) of SOA is presented in Fig. A1. The CP predicts a decrease in $T_{g,org}$ for C_{8-12} with the lowest $T_{g,org}$ of ~250 K, which is likely due to a decrease of O:C ratio (Fig. 1d) as lower O:C ratio can lead to a decrease of T_g (DeRieux et al., 2018; Shiraiwa et al., 2017), followed by an increase of $T_{g,org}$ with n to reach ~270 K with C_{17}. These values correspond to viscosity of 10^4 - 10^6 Pa s, indicating that n-alkane SOA adopts viscous semisolid phase state. The increase of viscosity for larger precursors is apparently reasonable, as their oxidation products would have higher molar mass which would generally correspond to higher $T_{g,org}$ (Koop et al., 2011; Shiraiwa et al., 2017). Based on the Stokes-Einstein relation, bulk diffusivity would be in the range of 3×10^{-15} - 10^{-12} cm^2 s^{-1}. The characteristic timescale of bulk diffusion in an average particle diameter of 300 nm can be as low as ~2 hours (Shiraiwa et al., 2011), which is longer than experimental timescale of one hour. These low diffusivities and long diffusion timescale can induce concentration gradients in the particle bulk, reducing α_{eff} to cause significant kinetic limitations to retard SOA growth, which is not consistent with the measured SOA yields.

tgBoost predicts the opposite trend, predicting a monotonic decrease of $T_{g,org}$ and viscosity with an increase of n, suggesting that SOA phase state shifts from an amorphous semisolid state ($10^2 < \eta < 10^5$ Pa s) towards a liquid-like phase state ($\eta < 10^2$ Pa s). These results are counter-intuitive as T_g values of n-alkanes increase with an increase of n, which can be reproduced with great precision by tgBoost (Galeazzo and Shiraiwa, 2022). The determinants explaining this unexpected trend are chemical composition and molecular structure of the oxidation products as discussed below. The characteristic timescale of bulk diffusion is less than one second in a low viscous state and high bulk diffusivity (Shiraiwa et al., 2011) and SOA particles are expected be homogeneously well-mixed. Hence, α_{eff} remains very close to 1 with little kinetic limitation of bulk diffusion.

318   Unfortunately, no direct viscosity measurements of n-alkane SOA generated under high
319   NO_x conditions are available to date, while there are two studies for n-alkane SOA generated
320   under NOx-free conditions. Saukko et al. (2012) (Saukko et al., 2012) observed that n-
321   heptadecane ($C_{17}H_{36}$) SOA with low O:C ratio did not bounce from an impactor plate. It
322   indicates that these particles adopted a liquid-like state, as indicated by the violet shading in
323   Fig. 2(a), which is consistent with the tgBoost prediction. Shiraiwa et al. (2013) estimated bulk
324   diffusivity of n-dodecane ($C_{12}H_{26}$) SOA generated without NO_x to be 10^{-12} cm^2 s^{-1} using a
325   kinetic multilayer model to simulate evolution of particle size distribution. While these two data
326   points cannot be directly compared with the viscosity predictions of high NOx n-alkane SOA,
327   they serve as reference data points for now and direct viscosity or bulk diffusivity
328   measurements of high NO_x n-alkane SOA are warranted in future studies.
329   Figure 2(b) shows the thermal desorption profiles of DOS that was present as seed
330   particles within the SOA formed from oxidation of the n-alkanes. Since DOS desorption
331   involved diffusion through the SOA prior to escape into vacuum, these profiles provided a
332   means for probing the SOA viscosity. The peaks in the DOS profiles for the C_{8-13} and C_{14-17} n-
333   alkanes are closely grouped, with vaporizer temperature at ~80 °C and ~65 °C, respectively,
334   with the peak for pure DOS occurring in between at ~72°C. The observed decrease in desorption
335   temperatures from low to high carbon numbers suggests an increase in effective volatility of
336   DOS in SOA generated from larger n-alkanes. In addition, Lim and Ziemann (2009) have
337   observed that C_{10} n-alkane SOA generated under high NOx conditions evaporate at higher
338   temperatures compared to C_{12} and C_{15} n-alkane SOA based on total ion thermal desorption
339   measurements (Lim and Ziemann, 2009b). Volatility and T_g were shown to exhibit clear
340   anticorrelation (Li et al., 2020); hence, these results strongly indicate that C_{8-13} SOA have higher
341   T_g and viscosity compared to C_{13-17} SOA. Note that the C_{13} profile is bimodal with peaks at
342   ~80 °C and ~65 °C (Fig. 2b), which is in line with tgBoost prediction that the viscosity of C_{13}
343   alkane SOA is at the edge of amorphous semi-solid and liquid phase states (Fig. 2a). These
344   results indicate that n-alkane SOA generated by larger precursors adopt low viscous liquid-like
345   states, while n-alkane SOA generated by smaller precursors adopt viscous semisolid states, in
346   agreement with tgBoost predictions. The major strength of tgBoost is that it considers molecular
347   structure and functionality for T_g predictions, while the compositional parameterization does
348   not account for this effect, leading to intuitive but erroneous predictions.
349
350   **Chemical composition of SOA.**

351   Figure 1 also shows the simulated (c) N:C and (d) O:C ratios of SOA with $\alpha = 1$ (black

352   line) and $\alpha = \alpha_{\text{eff}}$ with T_g determined with tgBoost (green line) or the compositional

353   parameterization (orange line). The N:C ratio is very similar among all simulations being ~0.2

354   for C_8 and decreasing progressively to ~0.03 with each addition of a carbon atom in the

355   precursor. O:C ratios were calculated in two different ways by treating a nitrate (-ONO$_2$) group

356   to contain either three (solid lines) or one (dashed lines) oxygen atoms. One oxygen atom is

357   also considered because O:C ratios reported from aerosol mass spectrometer measurements

358   generally treat a nitrate group the same as a hydroxyl group, since they have the same effect on

359   oxidation state (Farmer et al., 2010). Similar to the N:C ratio, there is a constant decrease in

360   O:C of SOA with increasing n, which is consistent with previous measurements for n-

361   pentadecane ($C_{15}H_{32}$) SOA (Aimanant and Ziemann, 2013a) and n-hexadecane ($C_{16}H_{34}$) SOA

362   in this study, even though the simulated values are ~45% and 15% lower than the measured

363   N:C and O:C ratios, respectively. The discrepancies are likely due to errors on modeling gas-

364   wall partitioning and gas-particle partitioning. The difference may also be caused by missing

365   processes in the model such as reactive uptake of oxidants and particle-phase chemistry.

366   We measured functional group distributions in n-hexadecane SOA using derivatization-

367   spectrophotometric methods described in Aimanant and Ziemann (2013b), as shown in Fig.

368   1(b) and summarized in Table A1. Experimental measurements report high presence of -CH$_2$-

369   (13.81) and -ONO$_2$ (0.91), followed by ROH (0.41), RC(=O) (0.38), and RC(=O)OR (0.28),

370   with the average measured number of groups per C_{16} molecule in parenthesis. Figure 1(b)

371   includes simulation results by GECKO-A with CP and tgBoost, showing overall satisfactory

372   agreement. The simulated results with tgBoost show excellent agreement for hydroxyl and

373   methylene groups, while the simulated nitrates and carbonyls (ketones + aldehydes) are lower

374   than the measurements. The simulation by CP has also a similar trend, but with significantly

375   lower presence of nitrates, carbonyls, and esters.

376   Figure 3(a) shows the top 15 oxidation products in the particle phase formed by the

377   oxidation of n-hexadecane simulated by GECKO-A box model with tgBoost. Note that

378   positional isomers are lumped into one species and that the five species in the first row

379   constitute majority (~86%) of SOA mass. The simulated SOA is composed mostly by 1st

380   generation products including alkyl nitrates, hydroxynitrates, and hydroxyketones. There is also

381   a significant presence of 2nd and 3rd generation products such as esters and dinitrates. We also

382   predicted multi-functionalized decomposition products including smaller chain hydroxy

383   nitrates and alkyl lactones as well as particle-phase products from cyclization of

384   hydroxyketones and dehydration of cyclic hemiacetals to form dihydrofurans. A very recent

study by Ranney et al. (2023) measured n-hexadecane oxidation products under high NOx, finding that alkyl nitrates, hydroxyl nitrates, hydroxyl carbonyls, cyclic hemiacetals, and cyclic hemiacetal nitrates were major products. These compounds are also major products as shown in Fig. 3a, suggesting that GECKO-A simulated n-alkane oxidation very well. There are notable differences in molecular composition for SOA simulated by CP compared to tgBoost (Fig. A2): the major compounds are 1st generation single and multi-functionalized products, followed by some 2nd and 3rd generation products, without decomposition products in the top species.

The simulated T_g by both methods for each compound are listed in Fig. 3. Overall tgBoost predicts T_g values between 157 – 221 K which are much lower compared to CP, especially with significant differences for organic nitrates and multi-functionalized species. As tgBoost considers the molecular structure, functional group and atomic interconnectivity of a molecule, it should make better predictions for multi-functionalized compounds based on the presence of different functional groups. CP is based on elemental composition and it predicts high T_g for compounds with high molar mass, predicting same T_g for isomers. In addition, the CP for CHON compounds was developed based on T_g values mainly estimated from their melting points, as there are limited number of CHON compounds with measured T_g available. T_g of organic nitrates are especially scarce and future T_g measurements for organic nitrates are desired to improve T_g parameterizations. For these reasons, CP overestimates T_g for oxidation products of n-alkane with long chain on average by ~66 K compared to tgBoost, overpredicting SOA viscosity as shown in Fig. 2(a).

Figure 3 also lists α_{eff} values, showing that they are very close to 1 for tgBoost, with SOA to be low viscous liquid with little kinetic limitations in mass accommodation. Additional oxidation products with lower concentrations are listed in Fig. A3 and their α_{eff} remain also close to 1. In contrast, as CP predicts the SOA phase state to be viscous amorphous semisolid, α_{eff} values for semi-volatile compounds become significantly smaller to kinetically limit mass accommodation. This decrease of α_{eff} is larger for compounds with higher volatility, as such compounds have higher re-evaporation rate on viscous particles with lower rate of bulk diffusion (Shiraiwa and Pöschl, 2021) (Fig. A3). α_{eff} for lower volatility compounds remain high, as they exhibit much lower desorption rates and are less likely to re-evaporate, even if their diffusion into the bulk is slow. Consequently, SOA simulated with CP mainly consists of later generation products with higher functionalization and molar masses.

Figure 3(b) shows top 15 oxidation products of n-decane ($C_{10}H_{26}$) as predicted by GECKO-A with tgBoost. SOA is mostly composed of 2nd and 3rd generation products with

multiple functional groups including nitrates, ketones, and alcohols. These highly oxidized products have T_g in the range of 225 – 304 K, with similar predictions by CP and tgBoost. This is consistent with previous studies that demonstrated successful applications of CP to predict the measured viscosity of SOA derived from biogenic and other relatively small precursors (DeRieux et al., 2018; Smith et al., 2021; Baboomian et al., 2022). These results are consistent with total ion thermal desorption profiles of n-alkane SOA formed in the presence of NOx (Lim and Ziemann, 2009b): C_{10} SOA was observed to have a broad single peak around ~75 °C, indicating the presence of low volatility multigenerational products; in contrast, C_{12} and C_{15} SOA exhibited two peaks with one larger peak at lower temperature, corresponding to 1st generation products and another smaller peak for multigenerational products. The phase state of n-decane SOA is predicted to be semisolid, but kinetic limitations are not strong as α_{eff} values for most compounds are only slightly reduced from 1.

Effects of mass loadings on viscosity.

The use of higher mass loadings in chamber experiments than ambient conditions assured that the condensation of semi-volatile vapors to suspended particles is a dominant process over vapor wall deposition (Zhang et al., 2014; Matsunaga and Ziemann, 2010). Chamber experiments of n-alkane photooxidation at high NO_x were also conducted with lower mass loading by Presto et al. (2010), who measured temporal evolution of SOA yields as shown in Fig. 4(a). SOA yields are increased with an increase of SOA mass concentrations, which is consistent with SOA absorptive partitioning theory (Pankow, 1994). The oxidation of larger precursors leads to higher SOA yields, in agreement with Lim and Ziemann (2009b) as presented in Fig. 1a. As shown with solid lines, the GECKO-A box model simulated experimental observations of SOA yields very well.

Figure 4(b) depicts the simulated SOA viscosity. We observed the same trend as Fig. 2(a) with lowering of viscosity upon an increase of carbon number n. SOA phase state is predicted to be semisolid for low carbon n, while it is expected to be liquid for high n. The predicted viscosity is about one order of magnitude higher compared to Fig. 2(a). Lower mass loadings suppress partitioning of higher volatility compounds, resulting in higher viscosity as condensation would be dominated by lower volatility compounds with higher T_g (Jain et al., 2018; Champion et al., 2019; Grayson et al., 2016; DeRieux et al., 2018).

Atmospheric Implications.

451   The phase state and viscosity of SOA formed by IVOCs have been largely unknown

452   and unexplored. We demonstrated in this study that SOA derived from small and middle size

453   n-alkanes (C_{12} and smaller) mostly consists of multigenerational oxidation products to adopt an

454   amorphous semisolid state, while larger n-alkane SOA are mainly composed of first generation

455   lightly oxidized products with one or two functional groups to adopt a low viscous liquid state.

456   This result is counter-intuitive, as it has been established that higher molar mass would lead to

457   higher glass transition temperature, and hence, higher viscosity (Koop et al., 2011; Shiraiwa et

458   al., 2017). In fact, the viscosity of biogenic SOA follows this trend: the viscosity of isoprene

459   (C_5H_8) SOA is reported to be lower than monoterpene ($C_{10}H_{16}$, such as α-pinene and limonene)

460   SOA (Renbaum-Wolff et al., 2013; Zhang et al., 2019), while oxidation products of

461   sesquiterpene ($C_{15}H_{24}$) increase viscosity of SOA (Smith et al., 2021), which is captured by

462   empirical parameterizations based on elemental composition (DeRieux et al., 2018; Li et al.,

463   2020). In contrast, n-alkane SOA exhibits an opposite trend, as indicated by thermal desorption

464   measurements that show that DOS in SOA formed by oxidation of large n-alkanes has higher

465   volatility. Hence, the SOA has lower viscosity, due to the enhanced presence of less

466   functionalized first-generation products (Li et al., 2020; Zhang et al., 2019). This trend is

467   successfully predicted by GECKO-A combined with machine learning-based model tgBoost,

468   which emphasizes the importance of consideration of functionality and molecular structure in

469   accurate predictions of T_g. The relationship between viscosity and composition is also reflected

470   in the atomic O:C and N:C ratios of n-alkane SOA, which decrease monotonically upon an

471   increase of carbon number of the n-alkane, since higher oxidation state and functionalization

472   can increase T_g (DeRieux et al., 2018; Koop et al., 2011; Shiraiwa et al., 2017; Saukko et al.,

473   2012).

474   IVOCs have gained growing attention for better characterization of urban air quality, as

475   they represent an important source of SOA as shown by chamber experiments (Aimanant and

476   Ziemann, 2013a; Lim and Ziemann, 2009b) and as observed in field observations (Gentner et

477   al., 2012; Li et al., 2022; Robinson et al., 2007; McDonald et al., 2018). While a few large-scale

478   aerosol models treat IVOC SOA to achieve better agreement with ambient measurements (de

479   Gouw et al., 2011; Li et al., 2022; Zhao et al., 2016), IVOC SOA is still highly uncertain in

480   terms of chemical composition and particle phase state and model parameters and treatments

481   for SOA formation and partitioning are poorly constrained. Our study provides critical insights

482   for these aspects, showing that n-alkane SOA formation under high NOx conditions (as usually

483   the case for ambient urban air) is dominated by gas-phase chemistry followed by partitioning.

484   As the generated SOA particles adopt a low viscous state, there is little kinetic limitations of

485 mass accommodation and bulk diffusion, which supports the application of equilibrium SOA
486 partitioning in the boundary layer. While the experiments and modeling were conducted for dry
487 conditions in this study, the phase state and viscosity of ambient n-alkane SOA would be
488 expected to be even lower under humid conditions due to hygroscopic growth and water acting
489 as plasticizer. Note that further experiments and model simulations are required for different
490 conditions for middle and upper free troposphere, as viscosity is expected to become higher
491 under low temperatures.

492 It is notable that the combination of tgBoost and GECKO-A box model successfully
493 simulates SOA yields, functional group distributions and phase state. This new model
494 represents a unique and comprehensive tool for simulating formation, partitioning and chemical
495 evolution of SOA, opening up a new avenue for analyzing complex interplay of gas-phase
496 chemistry and particle-phase processes and composition in SOA for detailed analysis and
497 interpretation of laboratory experiments and field observations. In addition, we propose to
498 pursue the application of this model as a basis for the development of a detailed master
499 mechanism of multiphase aerosol chemistry as well as for the derivation of simplified but
500 realistic parameterizations for air quality and climate models. In regional and global air quality
501 models, it is challenging and computationally very expensive to treat complex SOA multiphase
502 processes. Thus, such processes should be treated in efficient but effective way and the new
503 model shall serve as benchmark for the development of simplified SOA descriptions.

504

505

506 **Acknowledgements.** This work was also funded by U.S. Department of Energy (DE-
507 SC0018349), U.S. National Science Foundation (AGS-1654104) and the Campus France
508 (Make Our Planet Great Again short stay program grant, mopga-short-0000000116). In
509 addition, PZ acknowledges support from the National Science Foundation under grant AGS-
510 1750447.

511

512 **Authors contributions.** TG and MS designed the study. TG conducted model simulations and
513 data analysis. RV, MC, and BA developed the GECKO-A model. YL and PZ conducted
514 experimental measurements. All authors discussed the results. TG and MS wrote the manuscript
515 with contributions from all coauthors.

516 **Competing interests.** At least one of the (co-)authors is a member of the editorial board of
517 Atmospheric Chemistry and Physics.

518   **Code/Data availability.** The simulation data may be obtained from the corresponding author
519   upon request. The model tgBoost is available in Github (https://github.com/U0M0Z/tgpipe) and
520   in the homepage (https://azothai.ps.uci.edu/).
521

522
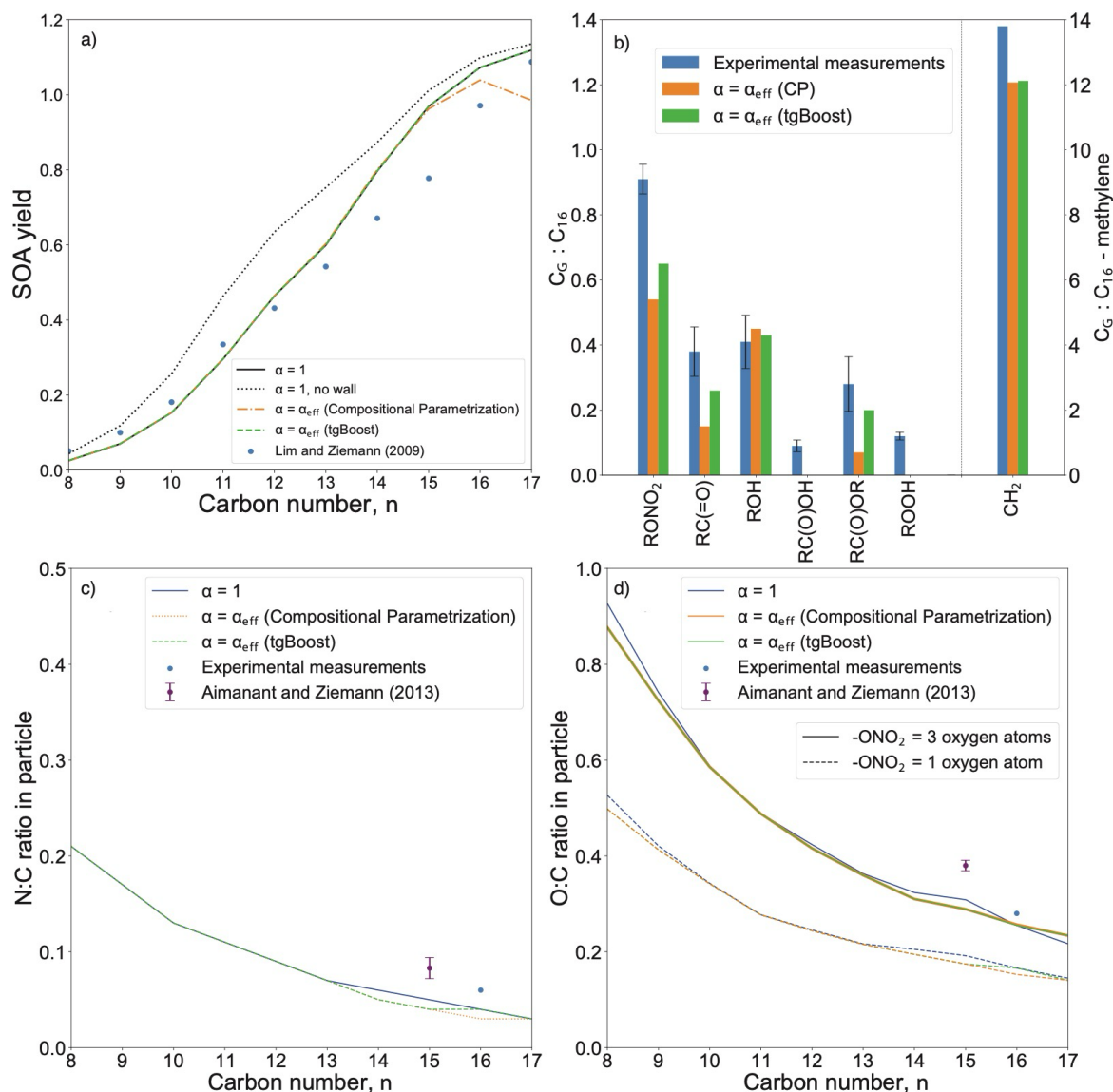
Figure 1: (a) Yields of SOA generated from OH oxidation of linear n-alkanes as measured by Lim and Ziemann (2009) (markers) (Lim and Ziemann, 2009b) and modeled by the GECKO-A box model (lines). The black line represents the base case with mass accommodation coefficient (α) of 1. The dashed lines represent simulations with effective mass accommodation coefficient (α_{eff}) as a function of bulk diffusivity from tgBoost (green) and the compositional parameterization (orange). (b) Simulated functional group distributions of n-hexadecane ($C_{16}H_{34}$) oxidation products in the particle phase. The blue bars represent experimental measurements. The green and orange bars represent GECKO-A box model simulations with α_{eff} with tgBoost and the compositional parameterization, respectively. (c) N:C and (d) O:C ratios in SOA formed by n-alkane oxidation simulated by the GECKO-A box model. The black line represents the base case with α of 1. The dashed lines represent simulations with α_{eff} with tgBoost (green) and the compositional parameterization (orange).

535
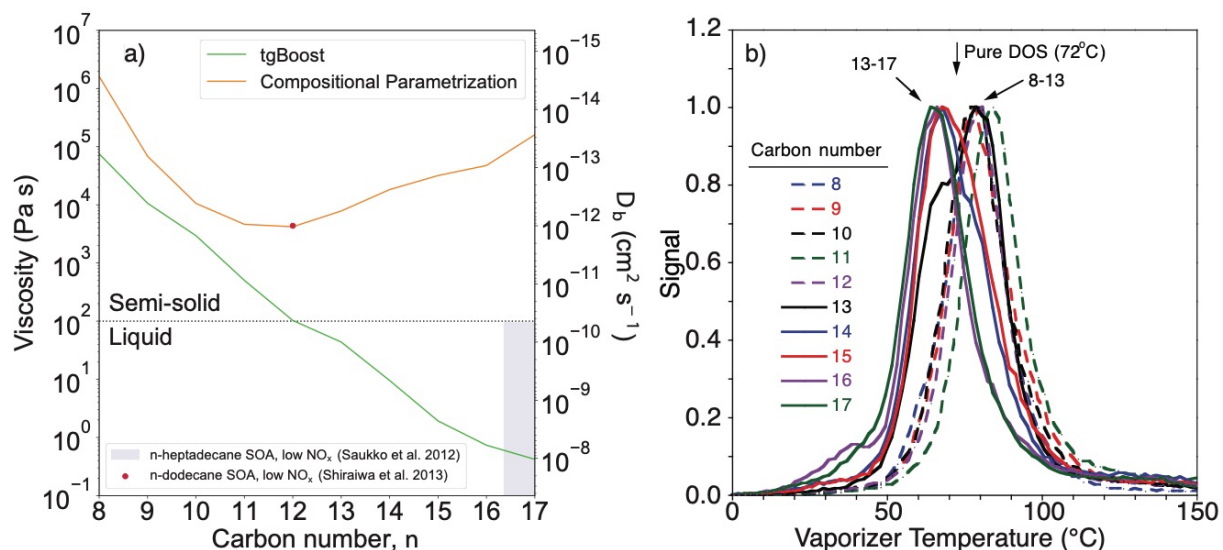
Figure 2: Phase state of n-alkane SOA. (a) Predicted viscosity of SOA generated from n-alkanes as computed by the GECKO-A box model with the T_g compositional parametrization (orange line) and tgBoost (green line) at the last step of the simulations (t = 3600 s). (b) Thermal desorption temperatures of dioctyl sebacate (DOS) that was present as seed particles in n-alkane SOA.
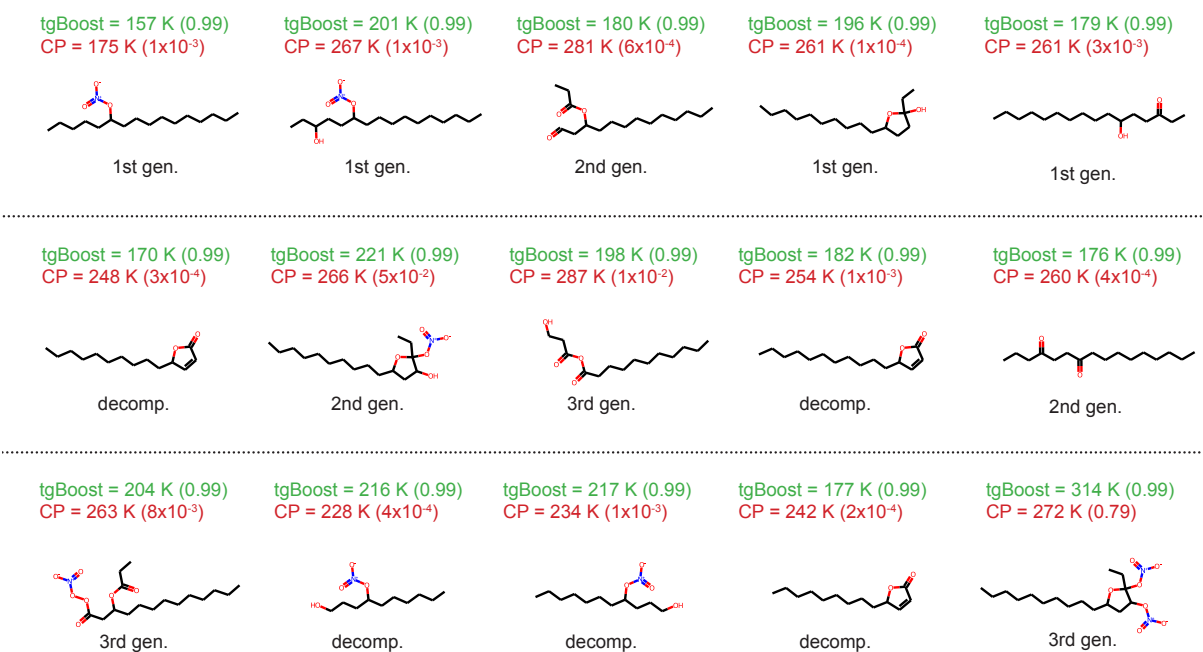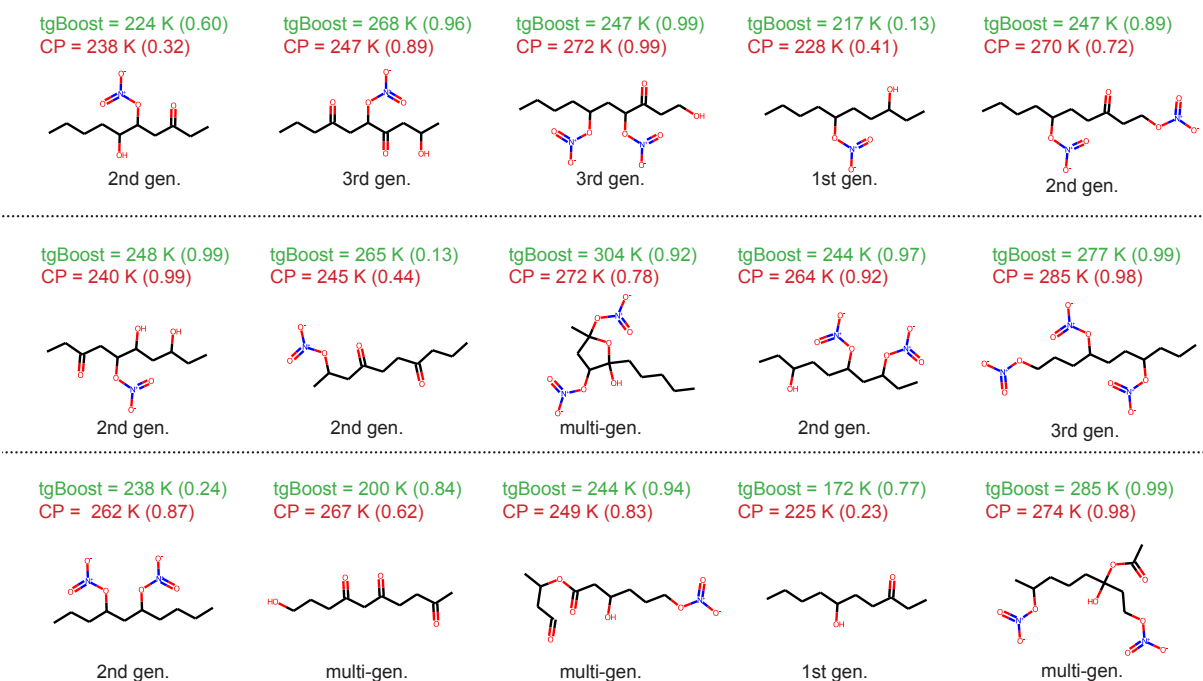
Figure 3: Molecular composition of oxidation products of n-alkanes under high NOx conditions in the particle phase. Top 15 SOA contributors with highest concentrations in (a) n-Hexadecane ($C_{16}H_{34}$) SOA and (b) n-Decane ($C_{10}H_{32}$) simulated by GECKO-A with effective mass accommodation coefficient (α_{eff}) with tgBoost. The species are reported in descending concentrations from left to right and from top to bottom. Positional isomers are lumped into one species. Listed values are T_g as calculated by tgBoost and CP and α_{eff} values at the end of simulation (3600 s) in brackets. Types of compounds are also noted (1st, 2nd, and 3rd generation products, decomposition products).
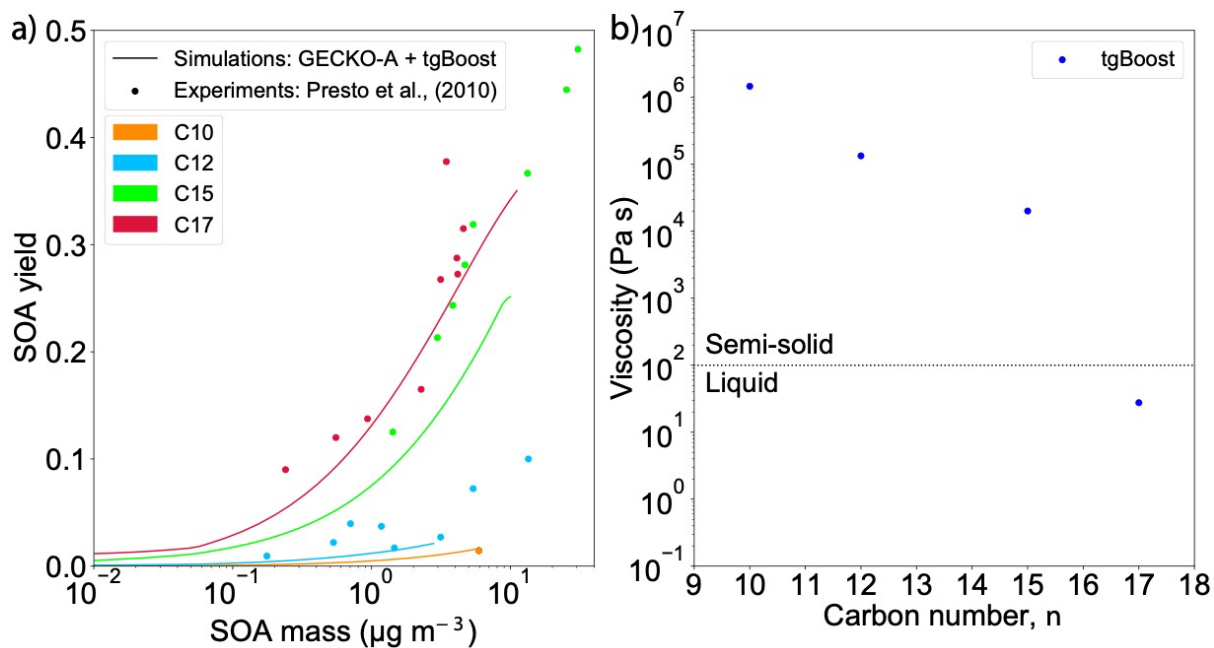
Figure 4: Effects of mass loadings on SOA yields and viscosity. (a) SOA yields from photo-oxidation of n-decane (C10), n-dodecane (C12), n-pentadecane (C15), and n-heptadecane (C17) at high NOx as a function of SOA mass concentration, as measured in Presto et al. (2010) (markers) and as modeled by the GECKO-A box model combined with tgBoost (lines). (b) SOA viscosity as modeled by the GECKO-A box model combined with tgBoost.

References.

Aimanant, S. and Ziemann, P. J.: Chemical Mechanisms of Aging of Aerosol Formed from the Reaction of n-Pentadecane with OH Radicals in the Presence of NOx, Aerosol Sci. Technol., 47, 979-990, 10.1080/02786826.2013.804621, 2013a.

Aimanant, S. and Ziemann, P. J.: Development of Spectrophotometric Methods for the Analysis of Functional Groups in Oxidized Organic Aerosol, Aerosol Sci. Technol., 47, 581-591, 10.1080/02786826.2013.773579, 2013b.

Atkinson, R., Carter, W. P. L., Winer, A. M., and Pitts, J. N.: An Experimental Protocol for the Determination of OH Radical Rate Constants with Organics Using Methyl Nitrite Photolysis as an OH Radical Source, Journal of the Air Pollution Control Association, 31, 1090-1092, 10.1080/00022470.1981.10465331, 1981.

Aumont, B., Szopa, S., and Madronich, S.: Modelling the evolution of organic carbon during its gas-phase tropospheric oxidation: development of an explicit model based on a self generating approach, Atmospheric Chemistry and Physics, 5, 2497-2517, 10.5194/acp-5-2497-2005, 2005.

Aumont, B., Valorso, R., Mouchel-Vallon, C., Camredon, M., Lee-Taylor, J., and Madronich, S.: Modeling SOA formation from the oxidation of intermediate volatility n-alkanes, Atmospheric Chemistry and Physics, 12, 7577-7589, 10.5194/acp-12-7577-2012, 2012.

Aumont, B., Camredon, M., Mouchel-Vallon, C., La, S., Ouzebidour, F., Valorso, R., Lee-Taylor, J., and Madronich, S.: Modeling the influence of alkane molecular structure on secondary organic aerosol formation, Faraday Discussions, 165, 105-122, 10.1039/C3FD00029J, 2013.

Baboomian, V. J., Crescenzo, G. V., Huang, Y., Mahrt, F., Shiraiwa, M., Bertram, A. K., and Nizkorodov, S. A.: Sunlight can convert atmospheric aerosols into a glassy solid state and modify their environmental impacts, Proc. Nat. Acad. Sci., 119, e2208121119, 10.1073/pnas.2208121119, 2022.

Bakker-Arkema, J. G. and Ziemann, P. J.: Minimizing Errors in Measured Yields of Particle-Phase Products Formed in Environmental Chamber Reactions: Revisiting the Yields of β-Hydroxynitrates Formed from 1-Alkene + OH/NOx Reactions, ACS Earth and Space Chemistry, 5, 690-702, 10.1021/acsearthspacechem.1c00008, 2021.

Champion, W. M., Rothfuss, N. E., Petters, M. D., and Grieshop, A. P.: Volatility and Viscosity Are Correlated in Terpene Secondary Organic Aerosol Formed in a Flow Reactor, Environmental Science & Technology Letters, 6, 513-519, 10.1021/acs.estlett.9b00412, 2019.

de Gouw, J. A., Middlebrook, A. M., Warneke, C., Ahmadov, R., Atlas, E. L., Bahreini, R., Blake, D. R., Brock, C. A., Brioude, J., Fahey, D. W., Fehsenfeld, F. C., Holloway, J. S., Le Henaff, M., Lueb, R. A., McKeen, S. A., Meagher, J. F., Murphy, D. M., Paris, C., Parrish, D. D., Perring, A. E., Pollack, I. B., Ravishankara, A. R., Robinson, A. L., Ryerson, T. B., Schwarz, J. P., Spackman, J. R., Srinivasan, A., and Watts, L. A.: Organic Aerosol Formation Downwind from the Deepwater Horizon Oil Spill, Science, 331, 1295-1299, 10.1126/science.1200320, 2011.

598 DeRieux, W. S. W., Li, Y., Lin, P., Laskin, J., Laskin, A., Bertram, A. K., Nizkorodov, S. A.,
599 and Shiraiwa, M.: Predicting the glass transition temperature and viscosity of secondary organic
600 material using molecular composition, Atmos. Chem. Phys., 18, 6331-6351, 10.5194/acp-18-
601 6331-2018, 2018.

602 Dette, H. P., Qi, M., Schröder, D. C., Godt, A., and Koop, T.: Glass-forming properties of 3-
603 Methylbutane-1,2,3-tricarboxylic acid and its mixtures with water and pinonic acid, The
604 Journal of Physical Chemistry A, 118, 7024-7033, 10.1021/jp505910w, 2014.

605 Docherty, K. S., Wu, W., Lim, Y. B., and Ziemann, P. J.: Contributions of organic peroxides
606 to secondary aerosol formed from reactions of monoterpenes with O_3, Environ. Sci. Technol.,
607 39, 4049-4059, 10.1021/es050228s, 2005.

608 Evoy, E., Maclean, A. M., Rovelli, G., Li, Y., Tsimpidi, A. P., Karydis, V. A., Kamal, S.,
609 Lelieveld, J., Shiraiwa, M., Reid, J. P., and Bertram, A. K.: Predictions of diffusion rates of
610 large organic molecules in secondary organic aerosols using the Stokes–Einstein and fractional
611 Stokes–Einstein relations, Atmos. Chem. Phys., 19, 10073-10085, 10.5194/acp-19-10073-
612 2019, 2019.

613 Farmer, D. K., Matsunaga, A., Docherty, K. S., Surratt, J. D., Seinfeld, J. H., Ziemann, P. J.,
614 and Jimenez, J. L.: Response of an aerosol mass spectrometer to organonitrates and
615 organosulfates and implications for atmospheric chemistry, Proc. Nat. Acad. Sci., 107, 6670-
616 6675, 2010.

617 Galeazzo, T. and Shiraiwa, M.: Predicting glass transition temperature and melting point of
618 organic compounds via machine learning and molecular embeddings, Environmental Science:
619 Atmospheres, 2, 362-374, 10.1039/D1EA00090J, 2022.

620 Galeazzo, T., Valorso, R., Li, Y., Camredon, M., Aumont, B., and Shiraiwa, M.: Estimation of
621 secondary organic aerosol viscosity from explicit modeling of gas-phase oxidation of isoprene
622 and α-pinene, Atmos. Chem. Phys., 21, 10199-10213, 10.5194/acp-21-10199-2021, 2021.

623 Gentner, D. R., Isaacman, G., Worton, D. R., Chan, A. W. H., Dallmann, T. R., Davis, L., Liu,
624 S., Day, D. A., Russell, L. M., Wilson, K. R., Weber, R., Guha, A., Harley, R. A., and Goldstein,
625 A. H.: Elucidating secondary organic aerosol from diesel and gasoline vehicles through detailed
626 characterization of organic carbon emissions, Proc. Nat. Acad. Sci., 109, 18318-18323,
627 10.1073/pnas.1212272109, 2012.

628 Grayson, J. W., Zhang, Y., Mutzel, A., Renbaum-Wolff, L., Böge, O., Kamal, S., Herrmann,
629 H., Martin, S. T., and Bertram, A. K.: Effect of varying experimental conditions on the viscosity
630 of α-pinene derived secondary organic material, Atmos. Chem. Phys., 16, 6027-6040,
631 10.5194/acp-16-6027-2016, 2016.

632 Grayson, J. W., Evoy, E., Song, M., Chu, Y., Maclean, A., Nguyen, A., Upshur, M. A.,
633 Ebrahimi, M., Chan, C. K., Geiger, F. M., Thomson, R. J., and Bertram, A. K.: The effect of
634 hydroxyl functional groups and molar mass on the viscosity of non-crystalline organic and
635 organic–water particles, Atmos. Chem. Phys., 17, 8509-8524, 10.5194/acp-17-8509-2017,
636 2017.

637 Jain, S., Fischer, B. K., and Petrucci, A. G.: The Influence of Absolute Mass Loading of
638 Secondary Organic Aerosols on Their Phase State, Atmosphere, 9, 10.3390/atmos9040131,
639 2018.

640 Jenkin, M. E., Valorso, R., Aumont, B., and Rickard, A. R.: Estimation of rate coefficients and
641 branching ratios for reactions of organic peroxy radicals for use in automated mechanism
642 construction, Atmos. Chem. Phys., 19, 7691-7717, 10.5194/acp-19-7691-2019, 2019.

643 Jenkin, M. E., Valorso, R., Aumont, B., Rickard, A. R., and Wallington, T. J.: Estimation of
644 rate coefficients and branching ratios for gas-phase reactions of OH with aliphatic organic
645 compounds for use in automated mechanism construction, Atmos. Chem. Phys., 18, 9297-9328,
646 10.5194/acp-18-9297-2018, 2018a.

647 Jenkin, M. E., Valorso, R., Aumont, B., Rickard, A. R., and Wallington, T. J.: Estimation of
648 rate coefficients and branching ratios for gas-phase reactions of OH with aromatic organic
649 compounds for use in automated mechanism construction, Atmos. Chem. Phys., 18, 9329-9349,
650 10.5194/acp-18-9329-2018, 2018b.

651 Jimenez, J. L., Canagaratna, M. R., Donahue, N. M., Prevot, A. S. H., Zhang, Q., Kroll, J. H.,
652 DeCarlo, P. F., Allan, J. D., Coe, H., Ng, N. L., Aiken, A. C., Docherty, K. S., Ulbrich, I. M.,
653 Grieshop, A. P., Robinson, A. L., Duplissy, J., Smith, J. D., Wilson, K. R., Lanz, V. A., Hueglin,
654 C., Sun, Y. L., Tian, J., Laaksonen, A., Raatikainen, T., Rautiainen, J., Vaattovaara, P., Ehn,
655 M., Kulmala, M., Tomlinson, J. M., Collins, D. R., Cubison, M. J., Dunlea, E. J., Huffman, J.
656 A., Onasch, T. B., Alfarra, M. R., Williams, P. I., Bower, K., Kondo, Y., Schneider, J.,
657 Drewnick, F., Borrmann, S., Weimer, S., Demerjian, K., Salcedo, D., Cottrell, L., Griffin, R.,
658 Takami, A., Miyoshi, T., Hatakeyama, S., Shimono, A., Sun, J. Y., Zhang, Y. M., Dzepina, K.,
659 Kimmel, J. R., Sueper, D., Jayne, J. T., Herndon, S. C., Trimborn, A. M., Williams, L. R.,
660 Wood, E. C., Middlebrook, A. M., Kolb, C. E., Baltensperger, U., and Worsnop, D. R.:
661 Evolution of organic aerosols in the atmosphere, Science, 326, 1525-1529,
662 10.1126/science.1180353, 2009.

663 Julin, J., Winkler, P. M., Donahue, N. M., Wagner, P. E., and Riipinen, I. A.: Near unity mass
664 accommodation coefficient of organic molecules of varying structure, Environ. Sci. Technol.,
665 48, 12083–12089, 10.1021/es501816h, 2014.

666 Knopf, D. A. and Alpert, P. A.: Atmospheric ice nucleation, Nat. Rev. Phys., 5, 203-217,
667 10.1038/s42254-023-00570-7, 2023.

668 Koop, T., Bookhold, J., Shiraiwa, M., and Pöschl, U.: Glass transition and phase state of organic
669 compounds: dependency on molecular properties and implications for secondary organic
670 aerosols in the atmosphere, Physical Chemistry Chemical Physics, 13, 19238-19255, 2011.

671 Krechmer, J. E., Pagonis, D., Ziemann, P. J., and Jimenez, J. L.: Quantification of gas-wall
672 partitioning in Teflon environmental chambers using rapid bursts of low-volatility oxidized
673 species generated in situ, Environ. Sci. Technol., 50, 5757-5765, 2016.

674 Kroll, J. H. and Seinfeld, J. H.: Chemistry of secondary organic aerosol: Formation and
675 evolution of low-volatility organics in the atmosphere, Atmos. Environ., 42, 3593-3624,
676 10.1016/j.atmosenv.2008.01.003, 2008.

677 La, Y. S., Camredon, M., Ziemann, P. J., Valorso, R., Matsunaga, A., Lannuque, V., Lee-
678 Taylor, J., Hodzic, A., Madronich, S., and Aumont, B.: Impact of chamber wall loss of gaseous
679 organic compounds on secondary organic aerosol formation: explicit modeling of SOA
680 formation from alkane and alkene oxidation, Atmospheric Chemistry and Physics, 16, 1417-
681 1431, 10.5194/acp-16-1417-2016, 2016.

Li, J. L., Li, K., Li, H., Wang, X. Z., Wang, W. G., Wang, K., and Ge, M. F.: Long-chain alkanes in the atmosphere: A review *, J. Environ. Sci., 114, 37-52, 10.1016/j.jes.2021.07.021, 2022.

Li, Y., Day, D. A., Stark, H., Jimenez, J. L., and Shiraiwa, M.: Predictions of the glass transition temperature and viscosity of organic aerosols from volatility distributions, Atmos. Chem. Phys., 20, 8103-8122, 10.5194/acp-20-8103-2020, 2020.

Lim, Y. B. and Ziemann, P. J.: Chemistry of Secondary Organic Aerosol Formation from OH Radical-Initiated Reactions of Linear, Branched, and Cyclic Alkanes in the Presence of NOx, Aerosol Sci. Technol., 43, 604-619, 10.1080/02786820902802567, 2009a.

Lim, Y. B. and Ziemann, P. J.: Effects of Molecular Structure on Aerosol Yields from OH Radical-Initiated Reactions of Linear, Branched, and Cyclic Alkanes in the Presence of NOx, Environ. Sci. Technol., 43, 2328-2334, 10.1021/es803389s, 2009b.

Maclean, A. M., Smith, N. R., Li, Y., Huang, Y., Hettiyadura, A. P. S., Crescenzo, G. V., Shiraiwa, M., Laskin, A., Nizkorodov, S. A., and Bertram, A. K.: Humidity-Dependent Viscosity of Secondary Organic Aerosol from Ozonolysis of β-Caryophyllene: Measurements, Predictions, and Implications, ACS Earth and Space Chemistry, 5, 305-318, 10.1021/acsearthspacechem.0c00296, 2021.

Matsunaga, A. and Ziemann, P. J.: Gas-wall partitioning of organic compounds in a Teflon film chamber and potential effects on reaction product and aerosol yield measurements, Aerosol Sci. Technol., 44, 881-892, 10.1080/02786826.2010.501044, 2010.

McDonald, B. C., de Gouw, J. A., Gilman, J. B., Jathar, S. H., Akherati, A., Cappa, C. D., Jimenez, J. L., Lee-Taylor, J., Hayes, P. L., McKeen, S. A., Cui, Y. Y., Kim, S.-W., Gentner, D. R., Isaacman-VanWertz, G., Goldstein, A. H., Harley, R. A., Frost, G. J., Roberts, J. M., Ryerson, T. B., and Trainer, M.: Volatile chemical products emerging as largest petrochemical source of urban organic emissions, Science, 359, 760, 2018.

Mu, Q., Shiraiwa, M., Octaviani, M., Ma, N., Ding, A., Su, H., Lammel, G., Pöschl, U., and Cheng, Y.: Temperature effect on phase state and reactivity controls atmospheric multiphase chemistry and transport of PAHs, Science Advances, 4, eaap7314, 2018.

Nannoolal, Y., Rarey, J., and Ramjugernath, D.: Estimation of pure component properties - Part 3. Estimation of the vapor pressure of non-electrolyte organic compounds via group contributions and group interactions, Fluid Phase Equilibria, 269, 117-133, 10.1016/j.fluid.2008.04.020, 2008.

O'Brien, R. E., Li, Y., Kiland, K. J., Katz, E. F., Or, V. W., Legaard, E., Walhout, E. Q., Thrasher, C., Grassian, V. H., DeCarlo, P. F., Bertram, A. K., and Shiraiwa, M.: Emerging investigator series: chemical and physical properties of organic mixtures on indoor surfaces during HOMEChem, Environmental Science: Processes & Impacts, 23, 559-568, 10.1039/D1EM00060H, 2021.

Pankow, J. F.: An absorption-model of the gas aerosol partitioning involved in the formation of secondary organic aerosol, Atmos. Environ., 28, 189-193, 1994.

721 Petters, S. S., Kreidenweis, S. M., Grieshop, A. P., Ziemann, P. J., and Petters, M. D.:
722 Temperature- and Humidity-Dependent Phase States of Secondary Organic Aerosols,
723 Geophysical Research Letters, 46, 1005-1013, 10.1029/2018GL080563, 2019.

724 Pöschl, U. and Shiraiwa, M.: Multiphase Chemistry at the Atmosphere–Biosphere Interface
725 Influencing Climate and Public Health in the Anthropocene, Chemical Reviews, 115, 4440–
726 4475, 10.1021/cr500487s, 2015.

727 Praske, E., Otkjær, R. V., Crounse, J. D., Hethcox, J. C., Stoltz, B. M., Kjaergaard, H. G., and
728 Wennberg, P. O.: Atmospheric autoxidation is increasingly important in urban and suburban
729 North America, Proc. Nat. Acad. Sci., 115, 64-69, 10.1073/pnas.1715540115, 2018.

730 Presto, A. A., Miracolo, M. A., Donahue, N. M., and Robinson, A. L.: Secondary organic
731 aerosol formation from high-NOx photo-oxidation of low volatility precursors: n-alkanes,
732 Environ. Sci. Technol., 44, 2029-2034, 10.1021/es903712r, 2010.

733 Pye, H. O. T., D'Ambro, E. L., Lee, B. H., Schobesberger, S., Takeuchi, M., Zhao, Y., Lopez-
734 Hilfiker, F., Liu, J., Shilling, J. E., Xing, J., Mathur, R., Middlebrook, A. M., Liao, J., Welti,
735 A., Graus, M., Warneke, C., de Gouw, J. A., Holloway, J. S., Ryerson, T. B., Pollack, I. B., and
736 Thornton, J. A.: Anthropogenic enhancements to production of highly oxygenated molecules
737 from autoxidation, Proc. Nat. Acad. Sci., 116, 6641, 10.1073/pnas.1810774116, 2019.

738 Ranney, A. P., Longnecker, E. R., Ziola, A. C., and Ziemann, P. J.: Measured and Modeled
739 Secondary Organic Aerosol Products and Yields from the Reaction of n-Hexadecane +
740 OH/NOx, ACS Earth and Space Chemistry, 7, 2298-2310,
741 10.1021/acsearthspacechem.3c00227, 2023.

742 Reid, J. P., Bertram, A. K., Topping, D. O., Laskin, A., Martin, S. T., Petters, M. D., Pope, F.
743 D., and Rovelli, G.: The viscosity of atmospherically relevant organic particles, Nature
744 Communications, 9, 956, 10.1038/s41467-018-03027-z, 2018.

745 Renbaum-Wolff, L., Grayson, J. W., Bateman, A. P., Kuwata, K., Sellier, M., Murray, B. J.,
746 Schilling, J. E., Martin, S. T., and Bertram, A. K.: Viscosity of α-pinene secondary organic
747 material and implications for particle growth and reactivity, Proceedings of the National
748 Academy of Sciences of the United States of America, 110, 8014-8019,
749 10.1073/pnas.1219548110 2013.

750 Robinson, A. L., Donahue, N. M., Shrivastava, M. K., Weitkamp, E. A., Sage, A. M., Grieshop,
751 A. P., Lane, T. E., Pierce, J. R., and Pandis, S. N.: Rethinking organic aerosols: Semivolatile
752 emissions and photochemical aging, Science, 315, 1259-1262, 10.1126/science.1133061, 2007.

753 Rothfuss, N. E. and Petters, M. D.: Influence of Functional Groups on the Viscosity of Organic
754 Aerosol, Environ. Sci. Technol., 51, 271-279, 10.1021/acs.est.6b04478, 2017.

755 Saukko, E., Lambe, A. T., Massoli, P., Koop, T., Wright, J. P., Croasdale, D. R., Pedernera, D.
756 A., Onasch, T. B., Laaksonen, A., Davidovits, P., Worsnop, D. R., and Virtanen, A.: Humidity-
757 dependent phase state of SOA particles from biogenic and anthropogenic precursors,
758 Atmospheric Chemistry and Physics, 12, 7517-7529, 10.5194/acp-12-7517-2012, 2012.

759 Schervish, M. and Shiraiwa, M.: Impact of phase state and non-ideal mixing on equilibration
760 timescales of secondary organic aerosol partitioning, Atmos. Chem. Phys., 23, 221-233,
761 10.5194/acp-23-221-2023, 2023.

762 Seinfeld, J. H. and Pandis, S. N.: Atmospheric chemistry and physics: from air pollution to
763 climate change, John Wiley & Sons2016.

764 Shiraiwa, M. and Pöschl, U.: Mass accommodation and gas–particle partitioning in secondary
765 organic aerosols: dependence on diffusivity, volatility, particle-phase reactions, and penetration
766 depth, Atmos. Chem. Phys., 21, 1565-1580, 10.5194/acp-21-1565-2021, 2021.

767 Shiraiwa, M., Ammann, M., Koop, T., and Pöschl, U.: Gas uptake and chemical aging of
768 semisolid organic aerosol particles, Proc. Nat. Acad. Sci., 108, 11003-11008,
769 10.1073/pnas.1103045108, 2011.

770 Shiraiwa, M., Berkemeier, T., Schilling-Fahnestock, K. A., Seinfeld, J. H., and Pöschl, U.:
771 Molecular corridors and kinetic regimes in the multiphase chemical evolution of secondary
772 organic aerosol, Atmos. Chem. Phys., 14, 8323-8341, 10.5194/acp-14-8323-2014, 2014.

773 Shiraiwa, M., Yee, L. D., Schilling, K. A., Loza, C. L., Craven, J. S., Zuend, A., Ziemann, P.
774 J., and Seinfeld, J. H.: Size distribution dynamics reveal particle-phase chemistry in organic
775 aerosol formation, Proceedings of the National Academy of Sciences of the United States of
776 America, 110, 11746-11750, 10.1073/pnas.1307501110, 2013.

777 Shiraiwa, M., Li, Y., Tsimpidi, A. P., Karydis, V. A., Berkemeier, T., Pandis, S. N., Lelieveld,
778 J., Koop, T., and Pöschl, U.: Global distribution of particle phase state in atmospheric secondary
779 organic aerosols, Nature Communications, 8, 15002, 10.1038/ncomms15002, 2017.

780 Shrivastava, M., Lou, S., Zelenyuk, A., Easter, R. C., Corley, R. A., Thrall, B. D., Rasch, P. J.,
781 Fast, J. D., Massey Simonich, S. L., Shen, H., and Tao, S.: Global long-range transport and lung
782 cancer risk from polycyclic aromatic hydrocarbons shielded by coatings of organic aerosol,
783 Proc. Nat. Acad. Sci., 114, 1246-1251, 2017.

784 Smith, N. R., Crescenzo, G. V., Huang, Y., Hettiyadura, A. P. S., Siemens, K., Li, Y., Faiola,
785 C. L., Laskin, A., Shiraiwa, M., Bertram, A. K., and Nizkorodov, S. A.: Viscosity and liquid–
786 liquid phase separation in healthy and stressed plant SOA, Environmental Science:
787 Atmospheres, 1, 140-153, 10.1039/D0EA00020E, 2021.

788 Song, M., Maclean, A. M., Huang, Y., Smith, N. R., Blair, S. L., Laskin, J., Laskin, A.,
789 DeRieux, W. S. W., Li, Y., Shiraiwa, M., Nizkorodov, S. A., and Bertram, A. K.: Liquid–liquid
790 phase separation and viscosity within secondary organic aerosol generated from diesel fuel
791 vapors, Atmos. Chem. Phys., 19, 12515-12529, 10.5194/acp-19-12515-2019, 2019.

792 Srivastava, D., Vu, T. V., Tong, S., Shi, Z., and Harrison, R. M.: Formation of secondary
793 organic aerosols from anthropogenic precursors in laboratory studies, npj Climate and
794 Atmospheric Science, 5, 22, 10.1038/s41612-022-00238-6, 2022.

795 Tobias, H. J., Kooiman, P. M., Docherty, K. S., and Ziemann, P. J.: Real-Time Chemical
796 Analysis of Organic Aerosols Using a Thermal Desorption Particle Beam Mass Spectrometer,
797 Aerosol Sci. Technol., 33, 170-190, 10.1080/027868200410912, 2000.

798 Valorso, R., Aumont, B., Camredon, M., Raventos-Duran, T., Mouchel-Vallon, C., Ng, N. L.,
799 Seinfeld, J. H., Lee-Taylor, J., and Madronich, S.: Explicit modelling of SOA formation from
800 α-pinene photooxidation: sensitivity to vapour pressure estimation, Atmospheric Chemistry and
801 Physics, 11, 6895-6910, 10.5194/acp-11-6895-2011, 2011.

Vereecken, L. and Peeters, J.: Decomposition of substituted alkoxy radicals—part I: a generalized structure–activity relationship for reaction barrier heights, Physical Chemistry Chemical Physics, 11, 9062-9074, 2009.

Verwer, J. G.: Gauss–Seidel iteration for stiff ODEs from chemical kinetics, SIAM Journal on Scientific Computing, 15, 1243-1250, 1994.

Verwer, J. G., Blom, J. G., and Hundsdorfer, W.: An implicit-explicit approach for atmospheric transport-chemistry problems, Applied Numerical Mathematics, 20, 191-209, 1996.

Virtanen, A., Joutsensaari, J., Koop, T., Kannosto, J., YliPirilä, P., Leskinen, J., Mäkelä, J. M., Holopainen, J. K., Pöschl, U., Kulmala, M., Worsnop, D. R., and Laaksonen, A.: An amorphous solid state of biogenic secondary organic aerosol particles, Nature, 467, 824-827, doi:10.1038/nature09455, 2010.

Ye, Q., Robinson, E. S., Ding, X., Ye, P., Sullivan, R. C., and Donahue, N. M.: Mixing of secondary organic aerosols versus relative humidity, Proc. Nat. Acad. Sci., 113, 12649-12654, 2016.

Zaveri, R. A., Wang, J., Fan, J., Zhang, Y., Shilling John, E., Zelenyuk, A., Mei, F., Newsom, R., Pekour, M., Tomlinson, J., Comstock Jennifer, M., Shrivastava, M., Fortner, E., Machado Luiz, A. T., Artaxo, P., and Martin Scot, T.: Rapid growth of anthropogenic organic nanoparticles greatly alters cloud life cycle in the Amazon rainforest, Science Advances, 8, eabj0329, 10.1126/sciadv.abj0329, 2022.

Zhang, X., Cappa, C. D., Jathar, S. H., McVay, R. C., Ensberg, J. J., Kleeman, M. J., and Seinfeld, J. H.: Influence of vapor wall loss in laboratory chambers on yields of secondary organic aerosol, Proc. Nat. Acad. Sci., 111, 5802-5807, 2014.

Zhang, Y., Chen, Y., Lambe, A. T., Olson, N. E., Lei, Z., Craig, R. L., Zhang, Z., Gold, A., Onasch, T. B., Jayne, J. T., Worsnop, D. R., Gaston, C. J., Thornton, J. A., Vizuete, W., Ault, A. P., and Surratt, J. D.: Effect of the Aerosol-Phase State on Secondary Organic Aerosol Formation from the Reactive Uptake of Isoprene-Derived Epoxydiols (IEPOX), Environmental Science & Technology Letters, 5, 167-174, 10.1021/acs.estlett.8b00044, 2018.

Zhang, Y., Nichman, L., Spencer, P., Jung, J. I., Lee, A., Heffernan, B. K., Gold, A., Zhang, Z., Chen, Y., Canagaratna, M. R., Jayne, J. T., Worsnop, D. R., Onasch, T. B., Surratt, J. D., Chandler, D., Davidovits, P., and Kolb, C. E.: The Cooling Rate- and Volatility-Dependent Glass-Forming Properties of Organic Aerosols Measured by Broadband Dielectric Spectroscopy, Environ. Sci. Technol., 53, 12366-12378, 10.1021/acs.est.9b03317, 2019.

Zhao, B., Wang, S., Donahue, N. M., Jathar, S. H., Huang, X., Wu, W., Hao, J., and Robinson, A. L.: Quantifying the effect of organic aerosol aging and intermediate-volatility emissions on regional-scale aerosol pollution in China, Sci. Rep., 6, 28815, 10.1038/srep28815, 2016.

Zhou, S., Hwang, B. C. H., Lakey, P. S. J., Zuend, A., Abbatt, J. P. D., and Shiraiwa, M.: Multiphase reactivity of polycyclic aromatic hydrocarbons is driven by phase separation and diffusion limitations, Proc. Nat. Acad. Sci., 116, 11658-11663, 10.1073/pnas.1902517116, 2019.

Ziemann, P. J. and Atkinson, R.: Kinetics, products, and mechanisms of secondary organic aerosol formation, Chemical Society Reviews, 41, 6582-6605, 2012.

843   Zobrist, B., Marcolli, C., Pedernera, D. A., and Koop, T.: Do atmospheric aerosols form
844   glasses?, Atmospheric Chemistry and Physics, 8, 5221-5244, 2008.
845
846

 Appendix.

848

849 **Table A1:** Experimental and simulated functional group distributions, O:C and N:C ratios of
850 SOA generated from C16 oxidation by OH in presence of high NO_x.

FG/C16 molecule	Experimental	Simulated (tgBoost)	Simulated (CP)
Nitrate	0.91	0.65	0.54
Carbonyl	0.38	0.26	0.15
Hydroxyl	0.41	0.43	0.45
Carboxyl	0.09	0.0	0.0
Ester	0.28	0.2	0.07
Peroxide	0.12	0.01	0.0
Methylene	13.81	12.12	12.07
O:C	0.28	0.25	0.25
N:C	0.06	0.04	0.03
H:C	1.85	/	/
MW	294	/	/
Density (g cm^{-3})	1.10	1.06	1.06

851

852

853
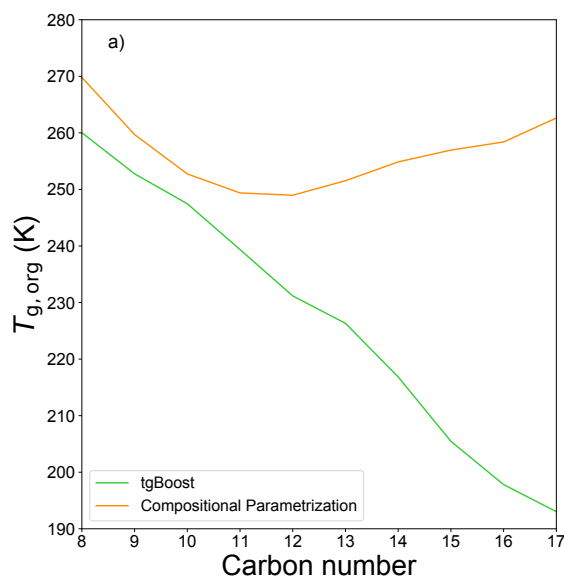
854
855 **Figure A1:** Predicted $T_{g,org}$ of SOA generated from n-alkanes as computed by the GECKO-A
856 box model with the T_g compositional parametrization (orange line) and tgBoost (green line) at
857 the last step of the simulations (t = 3600 s).
858

CP = 272 K (3x10⁻²) tgBoost = 195 K (0.99) — 1st gen.
CP = 267 K (0.78) tgBoost = 201 K (1.0) — 1st gen.
CP = 225 K (2x10⁻³) tgBoost = 165 K (0.86) — 2nd gen.
CP = 261 K (6x10⁻³) tgBoost = 196 K (0.99) — 1st gen.
CP = 261 K (0.14) tgBoost = 179 K (1.0) — 1st gen.

CP = 281 K (1x10⁻²) tgBoost = 180 K (0.99) — 2nd gen.
CP = 260 K (1x10⁻²) tgBoost = 186 K (0.99) — 2nd gen.
CP = 268 K (0.74) tgBoost = 230 K (1.0) — 3rd gen.
CP = 266 K (0.97) tgBoost = 239 K (1.0) — 2nd gen.
CP = 281 K (2x10⁻²) tgBoost = 188 K (0.99) — 2nd gen.

CP = 265 K (0.65) tgBoost = 221 K (1.0) — 2nd gen.
CP = 263 K (0.16) tgBoost = 205 K (1.0) — 2nd gen.
CP = 287 K (0.41) tgBoost = 198 K (1.0) — 3rd gen.
CP = 263 K (0.16) tgBoost = 211 K (1.0) — 2nd gen.
CP = 265 K (2x10⁻⁴) tgBoost = 249 K (0.88) — 3rd gen.

Figure A2. Top 15 species with highest concentrations in oxidation products of n-hexadecane ($C_{16}H_{34}$) under high NOx conditions simulated by GECKO-A with effective mass accommodation coefficient (α_{eff}) with the compositional parameterization. The species are reported in descending concentrations from left to right and from top to bottom. Listed values are T_g as calculated by tgBoost and CP and α_{eff} values at the end of simulation (3600 s) in brackets. Types of compounds are also noted (1st, 2nd, and 3rd generation products, decomposition products).

868
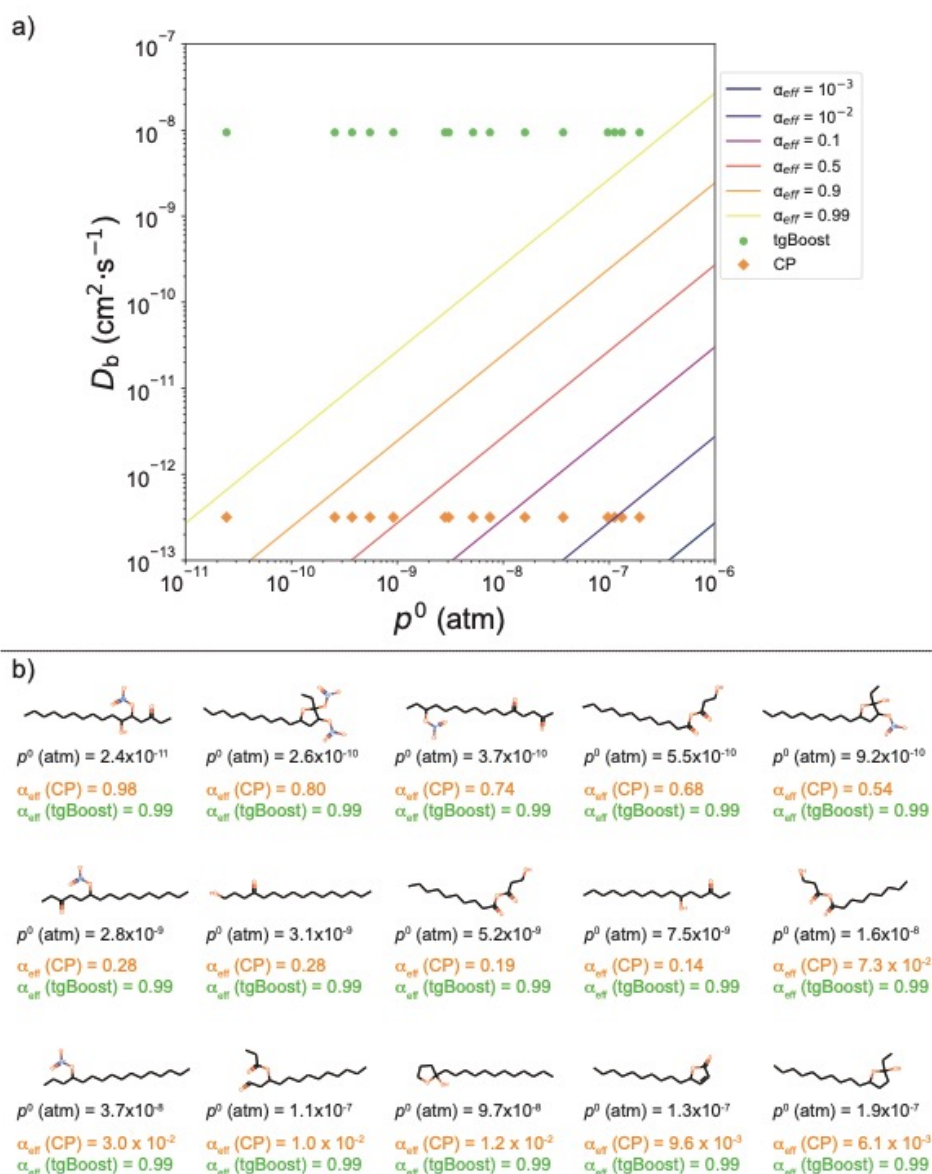
Figure A3. a) α_{eff} isolines as a function of bulk diffusivity D_{b} and saturation vapor pressure p^{o} of semi-volatile species. b) Selection of various representative SOA contributors produced during the oxidation of n-hexadecane. The species are ordered by decreasing vapor pressure. The reported α_{eff} values for each SOA contributor are calculated for D_{b} estimated with tgBoost ($D_{\mathrm{b}} = 1\times10^{-8}$ cm^2 s^{-1}) and CP ($D_{\mathrm{b}} = 3\times10^{-13}$ cm^2 s^{-1}). The values of α_{eff} for the selected species are reported as points in the top panel. It shows that for the liquid-like state estimated with the tgBoost configuration, α_{eff} tend towards 1 for all species. This behavior is not observed in the amorphous semi-solid state estimated using the CP model configuration for species with p^{o} above 10^{-9} atm. For the simulated conditions, species with p^{o} between 10^{-8} and 10^{-6} atm are of enough low volatility to partition between the particle and gas phases at equilibrium. For species in that volatility range, no mass transfer limitation is observed with the tgBoost configuration, unlike the CP configuration. Using the CP configuration, the most volatile SOA contributors are subjected to substantial mass transfer limitation and are therefore mainly eliminated by gas-phase oxidation or wall deposition.

883